Misfit strain-temperature phase diagrams and domain stability of asymmetric ferroelectric capacitors: Thermodynamic calculation and phase-field simulation

W. J. Chen, Yue Zheng', B. Wang', D. C. Ma, and C. M. Wu

Citation: Journal of Applied Physics **115**, 094101 (2014); doi: 10.1063/1.4867480
View online: http://dx.doi.org/10.1063/1.4867480
View Table of Contents: http://aip.scitation.org/toc/jap/115/9
Published by the American Institute of Physics

Misfit strain-temperature phase diagrams and domain stability of asymmetric ferroelectric capacitors: Thermodynamic calculation and phase-field simulation

W. J. Chen,[1,2] Yue Zheng,[1,2,a)] B. Wang,[1,b)] D. C. Ma,[1] and C. M. Wu[1,2]
[1]*State Key Laboratory of Optoelectronic Materials and Technologies, School of Physics and Engineering, Sun Yat-sen University, 510275 Guangzhou, China*
[2]*Micro&Nano Physics and Mechanics Research Laboratory, School of Physics and Engineering, Sun Yat-sen University, 510275 Guangzhou, China*

(Received 9 September 2013; accepted 20 February 2014; published online 4 March 2014)

Thermodynamic calculation and phase-field simulation have been conducted to investigate the misfit strain-temperature phase diagrams, dielectric property, and domain stability of asymmetric ferroelectric capacitors (FCs), with considering the effects of dissimilar screening properties and work function steps at the two interfaces. The distinct features of asymmetric FCs from their symmetric counterparts have been revealed and discussed. Polar states with nonzero out-of-plane polarization in parallel with the built-in field are found preferential to form in asymmetric FCs. Meanwhile, the built-in field breaks the degeneracy of states with out-of-plane polarization in anti-directions. This leads to the necessity of redefining phases according to the bistability of out-of-plane polarization. Moreover, the phase stability as well as the dielectric behavior can be significantly controlled by the properties of electrodes, misfit strain, and temperature. The phase-field simulation result also shows that polydomain instability would happen in asymmetric FCs as the equivalence of domain stability in anti-directions is destroyed. © *2014 AIP Publishing LLC*. [http://dx.doi.org/10.1063/1.4867480]

I. INTRODUCTION

Recently, nanoscale ferroelectric heterostructures, such as ferroelectric tunnel junctions (FTJs) and ferroelectric capacitors (FCs), have attracted significant attentions for their promising applications in advanced electronic devices. By exploiting the functionalities of ferroelectric thin film (FTF) and their influence on other properties (e.g., electronic transport), various important phenomena in FTJs or FCs, such as nonvolatile memory,[1] giant electroresistance (GER),[2,3] resistive switching,[4,5] giant piezoelectric resistance (GPR),[6,7] photovoltaic effects,[8] etc., have been revealed.

For a FTF at the nanoscale, its polarization state and thus the polarization relative properties can be affected by complicated factors.[9–27] In particular, the strain state of the FTF and the electromechanical environment in the vicinity of surfaces/interfaces, e.g., chemical bondings, interfacial work function step, and screening charges distribution in electrodes, could significantly affect the overall ferroelectric size effect. For example, the existence of ferroelectric critical thickness of FTFs has been theoretically investigated by first-principle calculations[9–13,15,19] and thermodynamic approaches,[20,21] and has also been explored in experiments.[24–27] Interestingly, even for films made of the same ferroelectric material, the reported critical thickness is found in a dispersive range and shows sensitivity to the details of surface/interface and strains. An abnormal enhancement of ferroelectricity and even a vanishing of ferroelectric critical thickness in FTFs have been recently shown to be possible through adjusting the interfacial chemical bondings.[16,18,19]

Generally speaking, the dissimilarity between the two electrode/FTF interfaces imposes asymmetry to the system. This asymmetry can bring about distinct features to the asymmetric FTJs and FCs from their symmetric counterparts. Indeed, a GER effect in asymmetric FTJs due to the different screening abilities of electrodes has been demonstrated.[2,3] Another important feature of asymmetric FTJs and FCs resides in the built-in electric field induced by asymmetric interfacial properties,[14,17,19,22,23] which breaks the degeneracy of states with out-of-plane polarization in anti-directions. Consequently, effects such as imprint behavior, shifted hysteresis loops, and smearing of phase transition are expected. As an important indication, a decrease and even vanishing of critical thickness for one polarization direction (and correspondingly an increase of critical thickness for the other polarization direction) would happen in asymmetric FTJs and FCs. These additional asymmetry-related features in asymmetric FTJs and FCs should have important implications on their applications. For example, the broken degeneracy of polarization states can lead to a loss of polarization bistability, which is crucial for applications based on polarization reversal such as memory. Therefore, it is important to reveal the distinct behaviors of asymmetric FTJs and FCs from both theoretical and experimental studies.

In literature, the "misfit strain-temperature" phase diagrams of epitaxial FTFs have been investigated using modified thermodynamic models[28,29] and phase-field simulations.[30] Recently, the phase diagrams of symmetric FCs affected by

a)Author to whom correspondence should be addressed. Electronic mail: zhengy35@mail.sysu.edu.cn.
b)Electronic mail: wangbiao@mail.sysu.edu.cn.

 © 2014 AIP Publishing LLC

electrode screening have been calculated, showing significant controllability of electrode on the phase boundaries.[31] Owing to the fact that FCs are usually in asymmetric geometries in practical applications and should exhibit distinct features from the symmetric counterparts, in this paper we combine thermodynamic calculation and phase-field simulation to investigate the phase diagrams, dielectric property, and domain stability of asymmetric FCs. The effects of dissimilar screening capabilities and work function steps of the two interfaces are taken into account. Important features of asymmetric FCs, such as the preferential formation of polar states, appearance of new phases, shifting of phase boundaries, dielectric smearing, and polydomain instability, etc., will be demonstrated and discussed.

II. THE PHYSICAL MODEL

The configuration of a model asymmetric FC with FTF of thicknesses h sandwiched between two dissimilar electrodes (e.g., Pt and $SrRuO_3$) is shown in Fig. 1. Under the short-circuit boundary condition, compensation charges with screening length being l_{e1} and l_{e2} are induced in electrode-1 and electrode-2, respectively. The spontaneous polarization $\mathbf{P}=(P_1, P_2, P_3)$ is defined as the polarization from permanent electric moment.[32–34] The electric displacement field can then be expressed in terms of the linear and nonlinear parts as $\mathbf{D}=\varepsilon_0\mathbf{E}+\boldsymbol{\chi}_\mathbf{b}\mathbf{E}+\mathbf{P}=\boldsymbol{\varepsilon}_\mathbf{b}\mathbf{E}+\mathbf{P}$, where $\boldsymbol{\chi}_\mathbf{b}$ and $\boldsymbol{\varepsilon}_\mathbf{b}$ are the background susceptibility and the dielectric constant tensor of the background materials, respectively, and $\mathbf{E}$ is the total electric field.[32,33] Since the background material is the paraelectric phase of cubic crystal symmetry, the background dielectric constants in three axis directions are the same, i.e., $\varepsilon_{11b}=\varepsilon_{22b}=\varepsilon_{33b}=\varepsilon_b$.

Taking a paraelectric crystal in the absence of surfaces and applied fields (i.e., electric, magnetic or mechanical, etc.) as the thermodynamic reference, the free energy of a FC can be regarded as the sum of the following components:

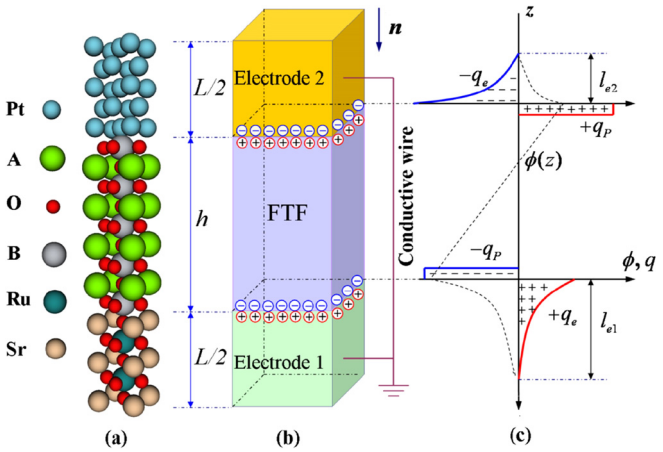

FIG. 1. (a) Atomic structures of a model asymmetric FC with Pt and $SrRuO_3$ electrodes, (b) its schematic configuration, and (c) charge distribution and potential profile under short-circuit boundary condition.

$$F=\int_V (f_{\text{bulk}}+f_{\text{elas}}+f_{\text{grad}}+f_{\text{elec}})dV+\int_S f_{\text{surf}}dS, \quad (1)$$

where f_{bulk}, f_{elas}, f_{grad}, f_{elec}, and f_{surf} are the densities of bulk Landau free energy, elastic energy, gradient energy, electrostatic energy, and surface energy, respectively. V and S are the occupied space and the surface of the ferroelectric, respectively.

A. Thermodynamic calculation

In the calculation of phase diagram and dielectric property of the capacitor, we assume a single-domain FTF with homogeneous polarization. Thus, the gradient energy is neglected, i.e., $f_{\text{grad}}=0$. Taking into account the effect of misfit strain, the sum of bulk Landau free energy f_{bulk} and elastic energy f_{elas} of a FTF is given by the following modified thermodynamic potential:[28,31]

$$\begin{aligned}f_{\text{bulk}}+f_{\text{elas}}=&\alpha_1^*(P_1^2+P_2^2)+\alpha_3^*P_3^2+\alpha_{11}^*(P_1^4+P_2^4)+\alpha_{33}^*P_3^4+\alpha_{13}^*(P_1^2+P_2^2)P_3^2\\&+\alpha_{12}^*P_1^2P_2^2+\alpha_{112}\left[P_1^4(P_2^2+P_3^2)+P_2^4(P_1^2+P_3^2)+P_3^4(P_1^2+P_2^2)\right]\\&+\alpha_{111}(P_1^6+P_2^6+P_3^6)+\alpha_{123}P_1^2P_2^2P_3^2+\alpha_{1111}(P_1^8+P_2^8+P_3^8)\\&+\alpha_{1112}[P_1^6(P_2^2+P_3^2)+P_2^6(P_1^2+P_3^2)+P_3^6(P_1^2+P_2^2)]+\alpha_{1122}(P_1^4P_2^4\\&+P_2^4P_3^4+P_1^4P_3^4)+\alpha_{1123}(P_1^4P_2^2P_3^2+P_2^4P_1^2P_3^2+P_3^4P_1^2P_2^2)+(s_{11}+s_{12})^{-1}u_m^2,\end{aligned} \quad (2)$$

with u_m being the misfit strain, α_{ijk}, α_{ijkl} being the higher order stiffness coefficients, and α_i^*, α_{ij}^* being the renormalized stiffness coefficients due to the misfit strain, i.e.,

$$\begin{aligned}&\alpha_1^*=\alpha_1-u_m\frac{Q_{11}+Q_{12}}{s_{11}+s_{12}},\quad \alpha_3^*=\alpha_1-u_m\frac{2Q_{12}}{s_{11}+s_{12}},\\&\alpha_{11}^*=\alpha_{11}+\frac{1}{2(s_{11}^2-s_{12}^2)}[(Q_{11}^2+Q_{12}^2)s_{11}-2Q_{11}Q_{12}s_{12}],\quad \alpha_{33}^*=\alpha_{11}+\frac{Q_{12}^2}{s_{11}+s_{12}},\\&\alpha_{12}^*=\alpha_{12}-\frac{1}{s_{11}^2-s_{12}^2}[(Q_{11}^2+Q_{12}^2)s_{12}-2Q_{11}Q_{12}s_{11}]+\frac{Q_{44}^2}{2s_{44}},\quad \alpha_{13}^*=\alpha_{12}+\frac{Q_{12}(Q_{11}+Q_{12})}{s_{11}+s_{12}},\end{aligned} \quad (3)$$

where α_1, α_{ij} are the dielectric stiffness and second-order stiffness coefficients; s_{ij} and Q_{ij} are the elastic compliance coefficients and electrostrictive coefficients, respectively. Note that u_m which is induced by the lattice mismatch between film and substrate should be referenced with respect to high temperature paraelectric phase rather than low temperature ferroelectric phase. Moreover, misfit strain relaxation would happen for the thicker films through mechanisms such as interfacial dislocation generation, thus u_m ought to be considered as the thickness-dependent effective misfit strain.[34–36]

For asymmetric FCs, effects of the depolarization field and the built-in electric field due to the difference between the work function steps of the two interfaces should be considered. In the absence of external applied electric field, **E** is the sum of built-in electric field $\mathbf{E}_{bi}$ and depolarization field $\mathbf{E}_d$. As the x and y dimensions of the FTF are much larger than the z dimension, we can just consider the depolarization field along the z direction, i.e.,

$$E_d = -\frac{1}{\varepsilon_b}\left(1 - \frac{h\varepsilon_b^{-1}}{l_{e1}\varepsilon_{e1}^{-1} + l_{e2}\varepsilon_{e2}^{-1} + h\varepsilon_b^{-1}}\right)P_3 = -\frac{1}{\varepsilon_b}(1-\theta)P_3, \tag{4}$$

with $\theta \equiv h\varepsilon_b^{-1}\left(l_{e1}\varepsilon_{e1}^{-1} + l_{e2}\varepsilon_{e2}^{-1} + h\varepsilon_b^{-1}\right)^{-1}$ and ε_{e1}, ε_{e2} being the dielectric constants of electrode-1 and electrode-2, respectively.[21,23,25] The work function steps for the two interfaces are defined as $\Delta\varphi_1$ and $\Delta\varphi_2$ at $\mathbf{P}=0$. Then, the z-directed built-in electric field can be given by $E_{bi} = -\delta\varphi/h$, where $\delta\varphi$ is defined as $\delta\varphi \equiv \Delta\varphi_2 - \Delta\varphi_1$. Using the Landau and Lifshitz functional,[37] the electric energy density f_{elec} is expressed as

$$f_{\text{elec}} = -\mathbf{PE} - \frac{1}{2}\varepsilon_b\mathbf{E}^2. \tag{5}$$

For a FTF at the nanoscale, it is necessary to consider the surface energy, which contains contributions of the near-interface variation of polarization and the direct coupling between the polarization and the interfaces.[14,15] Retaining the two lowest terms of Taylor expansion, the surface energy density is given by

$$f_{\text{surf}} = (\zeta_{1i} - \zeta_{2i})P_i + \frac{1}{2}(\eta_{1i} + \eta_{2i})P_i^2, \tag{6}$$

where coefficients of the surface energy expansion for the two surfaces of FTF are denoted as ζ_{1i}, η_{1i} and ζ_{2i}, η_{2i} with respect to P_i, respectively. Note that in this homogenous polarization model, we actually tackle with a polarization that is some kind of effective or averaged. Consequently, the surface energy modifies the free energy of the FTF in a similar way with the electric energy in Eq. (5). It can be seen that the first term of Eq. (6) acts like a built-in field and the latter term acts like a depolarization-like field. Nevertheless, we should bear in mind that this surface term is actually of short-range origin and is different from the long-range electric term.

Minimizing the total free energy with respect to the polarization components, the equilibrium spontaneous polarizations can be solved by the following equations, i.e., $\partial F/\partial P_i = 0$. The dielectric constants ε_{ij} at small signals are identical to the reciprocal dielectric susceptibilities χ_{ij}, which can be calculated from the second partial derivatives of the free energy, i.e., $\chi_{ij} = \partial^2 F/\partial P_i \partial P_j$.

B. Phase-field simulation

FTFs generally exhibit domain structure due to the coexistence of different energetic equivalent polarization variants. In this section, we construct a phase-field model to investigate the feature of domain stability in asymmetric FCs. In this model, the temporal evolution of the spontaneous polarization field is described by the time-dependent Ginzburg-Landau (TDGL) equations, i.e.,

$$\frac{\partial P_i}{\partial t} = -M\frac{\delta F}{\delta P_i}, \tag{7}$$

where M is a kinetic coefficient and t is time.

For simplicity, we focus on the stability of c-phase domain pattern, i.e., 180° domain pattern, which is likely to form in FTF under compressive misfit strain condition. In general, the mechanical strain field of 180° domain pattern is inhomogeneous near the domain walls due to the abrupt changes in the polarization.[38] Particularly for 180° domain pattern in asymmetric FCs, the adjacent domains have different polarization magnitudes due to the built-in field, and should also give rise to a spatial distribution of the strain field. Nevertheless, to have a qualitative rather than quantitative exploration on the feature of domain stability in asymmetric FCs, in our phase-field model the mechanical strain field is simply regarded as homogeneous throughout the film and is controlled by the misfit strain. We believe that this approximation would give rise to an inaccuracy of the quantities, but would not alter the major conclusion. Then, the sum of bulk Landau free energy f_{bulk} and elastic energy f_{elas} can be still described by Eq. (2) in Sec. II A.

To capture the energy contribution of the domain walls to the total free energy, it is necessary to include the gradient energy. To the lowest order of the Taylor expansion, the gradient energy density is given by

$$\begin{aligned} f_{\text{grad}} = {} & \frac{1}{2}G_{11}(P_{1,1}^2 + P_{2,2}^2 + P_{3,3}^2) \\ & + G_{12}(P_{1,1}P_{2,2} + P_{2,2}P_{3,3} + P_{1,1}P_{3,3}) \\ & + \frac{1}{2}G_{44}[(P_{1,2} + P_{2,1})^2 + (P_{2,3} + P_{3,2})^2 \\ & + (P_{1,3} + P_{3,1})^2] + \frac{1}{2}G'_{44}[(P_{1,2} - P_{2,1})^2 \\ & + (P_{2,3} - P_{3,2})^2 + (P_{1,3} - P_{3,1})^2], \end{aligned} \tag{8}$$

where G_{11}, G_{12}, G_{44}, and G'_{44} are gradient energy coefficients, and $P_{i,j}$ denotes the derivative of the ith component of the polarization vector, P_i, with respect to the jth coordinate.

The electric energy density f_{elec} has the same expression given by Eq. (5), except that the z-directional depolarization field at each grid point is now dependent on the polarization distribution along the z direction,[39] i.e.,

$E_d(x,y,z) = -\left(P_3(x,y,z) - \theta\overline{P_3}\right)\varepsilon_b^{-1}$, where the average polarization is defined as $\overline{P_3}(x,y) \equiv h^{-1}\int_0^h P_3(x,y,z)dz$. Thus, the total electric field is given by

$$E(x,y,z) = E_d(x,y,z) + E_{bi} = -\frac{1}{\varepsilon_b}\left(P_3(x,y,z) - \theta\overline{P_3}\right) - \frac{\delta\varphi}{h}. \quad (9)$$

To mainly show the asymmetric effect of built-in field on the domain stability, for the phase-field simulation we use the effective extrapolation length δ_i^{eff} to describe the surface effect on polarization relaxation.[40,41] The surface energy density can be approximately given by

$$f_{surf} = \frac{D_{11}P_1^2}{2\delta_1^{eff}} + \frac{D_{22}P_2^2}{2\delta_2^{eff}} + \frac{D_{44}P_3^2}{2\delta_3^{eff}}, \quad (10)$$

where D_{11}, D_{22}, and D_{44} are the material coefficients related to the gradient energy coefficients.

III. RESULTS AND DISCUSSIONS

In the following, we consider FCs with $PbTiO_3$ and $BaTiO_3$ thin films sandwiched between asymmetric electrodes, such as $SrRuO_3/BaTiO_3/Pt$, $SrRuO_3/PbTiO_3/Pt$, etc. We mainly concern about the effects of dissimilar screening properties and work function steps at the two interfaces. Here, we would like to calculate the misfit strain-temperature phase diagrams using both the traditional $\mathbf{P}^6$ approximated potential[28] (with the largest compressive strain ~0.5%) and $\mathbf{P}^8$ approximated potential[42] (with the largest compressive strain ~1%) for $BaTiO_3$. Values of the expansion coefficients of the $\mathbf{P}^6$ approximated potential for $PbTiO_3$ and $BaTiO_3$, including the electrostrictive coefficients and the elastic compliance coefficients are from Ref. 28. Those of the $\mathbf{P}^8$ approximated potential for $BaTiO_3$ can be found in Ref. 42. Ratio of the screening length and dielectric constant is taken as $\eta_{e1} \equiv l_{e1}/\varepsilon_{e1} = 0.93\,\mathrm{F^{-1}m^2}$ and $\eta_{e2} \equiv l_{e2}/\varepsilon_{e2} = 1.33\,\mathrm{F^{-1}m^2}$ for $SrRuO_3$ and Pt electrodes, respectively.[6] We set $\zeta_{1i} = \zeta_{2i} = \zeta$ and $(\eta_{1i} + \eta_{2i}) \approx 2\eta$ in the surface term, with $\varepsilon_0\eta \approx 0.01 \times 10^{-10}\mathrm{m}$.[14,15,43] The background dielectric constant ε_b takes value of $\sim 50\varepsilon_0$.[32,33] In the phase-field simulation, we would like to take $PbTiO_3$ asymmetric capacitors as examples to show the effect of built-in field on the domain stability. A grid of $128 \times 128 \times n_z$ discrete points at a scale of $\Delta x = \Delta y = 1\,\mathrm{nm}$ and $\Delta z = 0.5\,\mathrm{nm}$ is employed, with n_z being the number of grid points in the film thickness direction. Periodic boundary condition is applied along the x and y

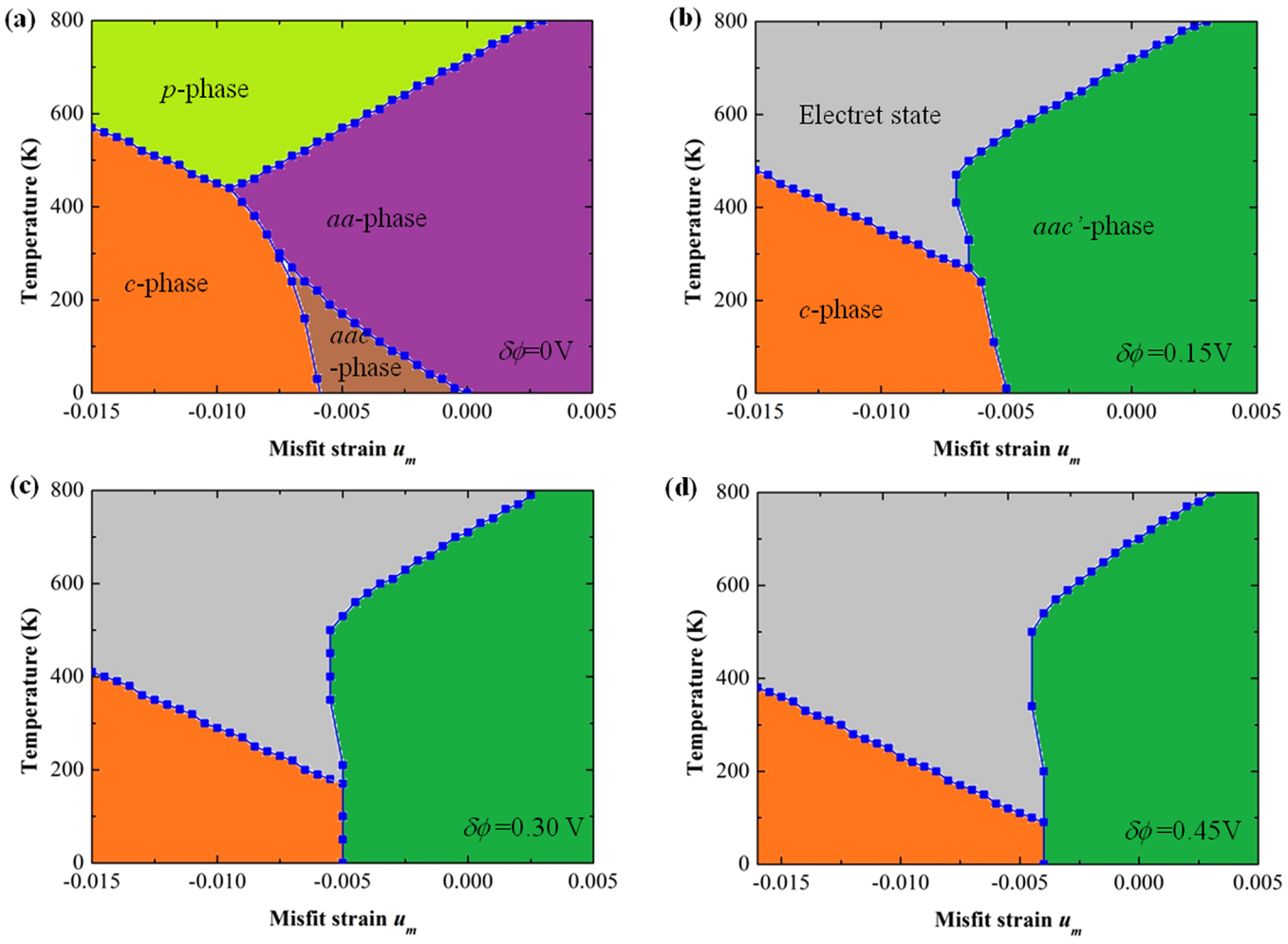

FIG. 2. Misfit strain-temperature phase diagram as a function of $\delta\varphi$ of asymmetric $Pt/PbTiO_3/SrRuO_3$ capacitor with 10 nm-thick $PbTiO_3$ thin film. (a) $\delta\varphi = 0\,\mathrm{V}$, (b) $\delta\varphi = 0.15\,\mathrm{V}$, (c) $\delta\varphi = 0.3\,\mathrm{V}$, and (d) $\delta\varphi = 0.45\,\mathrm{V}$.

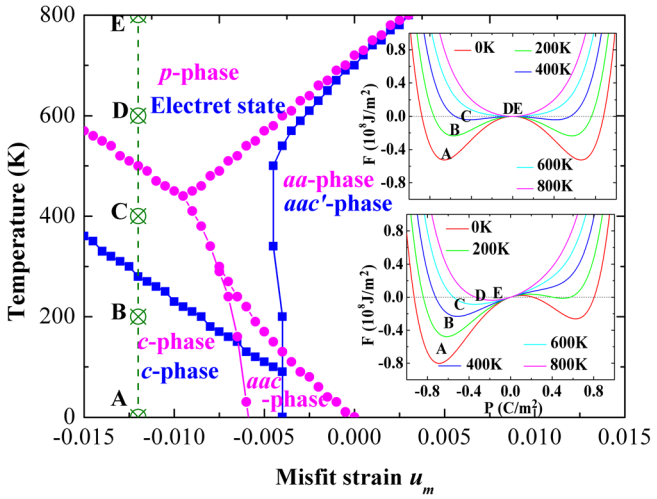

FIG. 3. Misfit strain-temperature phase diagrams of asymmetric $Pt/PbTiO_3/SrRuO_3$ capacitor with 10 nm-thick $PbTiO_3$ thin film in case of built-in field $\delta\varphi = 0$ V (pink circle lines) and $\delta\varphi = 0.45$ V (blue square lines). The upper inset ($\delta\varphi = 0$ V) and lower inset ($\delta\varphi = 0.45$ V) depict the free energy profiles of points A, B, C, D, and E along the line $u_m = -0.012$ with $T = 0$ K, 200 K, 400 K, 600 K, and 800 K.

directions. The extrapolation length δ_i^{eff} is chosen to be $\sim$2.8 nm.[41] The gradient energy coefficients are chosen to be $G_{11} = 0.6G_{110}$, $G_{12} = 0$, and $G_{44} = G'_{44} = 0.3G_{110}$, with $G_{110} = 1.73 \times 10^{-10}$ m^{4}NC^{-2}.

A. Misfit strain-temperature phase diagrams and dielectric property

We start our investigation on the effect of built-in field on the misfit strain-temperature phase diagrams of the capacitors. For asymmetric FCs, recent first-principle calculations have shown that the work function step difference $\delta\varphi$ depends not only on the bulk properties of the electrodes but also on the detailed bonding environment at the two interfaces.[19] Therefore, misfit strain-temperature phase diagrams of capacitors at various values of $\delta\varphi$ are calculated in order to more clearly understand the effect of asymmetric interfaces. The misfit strain-temperature phase diagrams of 10 nm-thick $PbTiO_3$ thin film sandwiched between dissimilar electrodes, i.e., $Pt/PbTiO_3/SrRuO_3$ capacitor, with $\delta\varphi = 0$ V, 0.15 V, 0.30 V, and 0.45 V, are calculated and shown in Fig. 2. Note

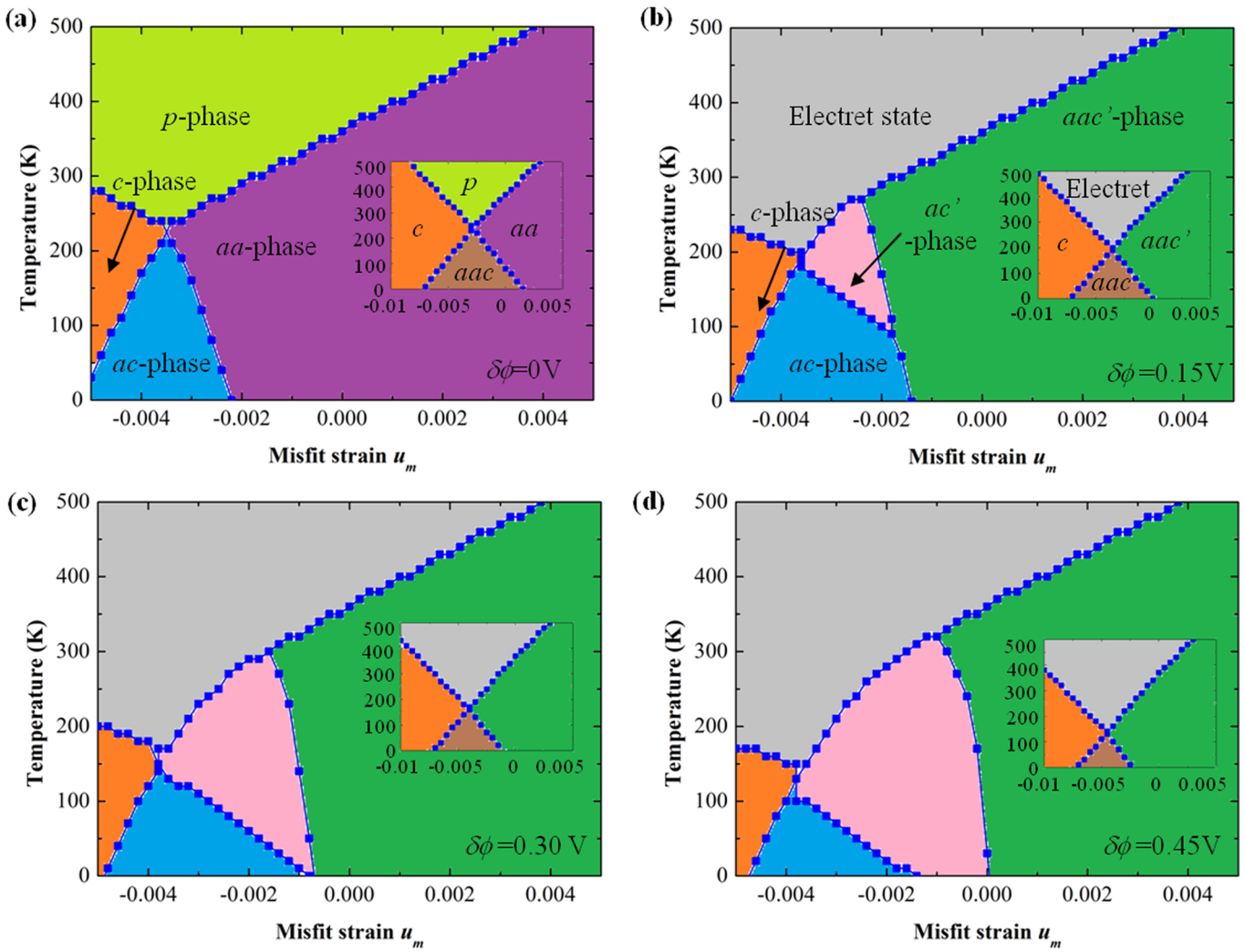

FIG. 4. Misfit strain-temperature phase diagram ($\mathbf{P}^6$ approximated potential) as a function of $\delta\varphi$ of asymmetric $Pt/BaTiO_3/SrRuO_3$ capacitor with 20 nm-thick $BaTiO_3$ thin film. (a) $\delta\varphi = 0$ V, (b) $\delta\varphi = 0.15$ V, (c) $\delta\varphi = 0.3$ V, and (d) $\delta\varphi = 0.45$ V. The inset figures depict the corresponding phase diagrams obtained by using the $\mathbf{P}^8$ approximated potential.

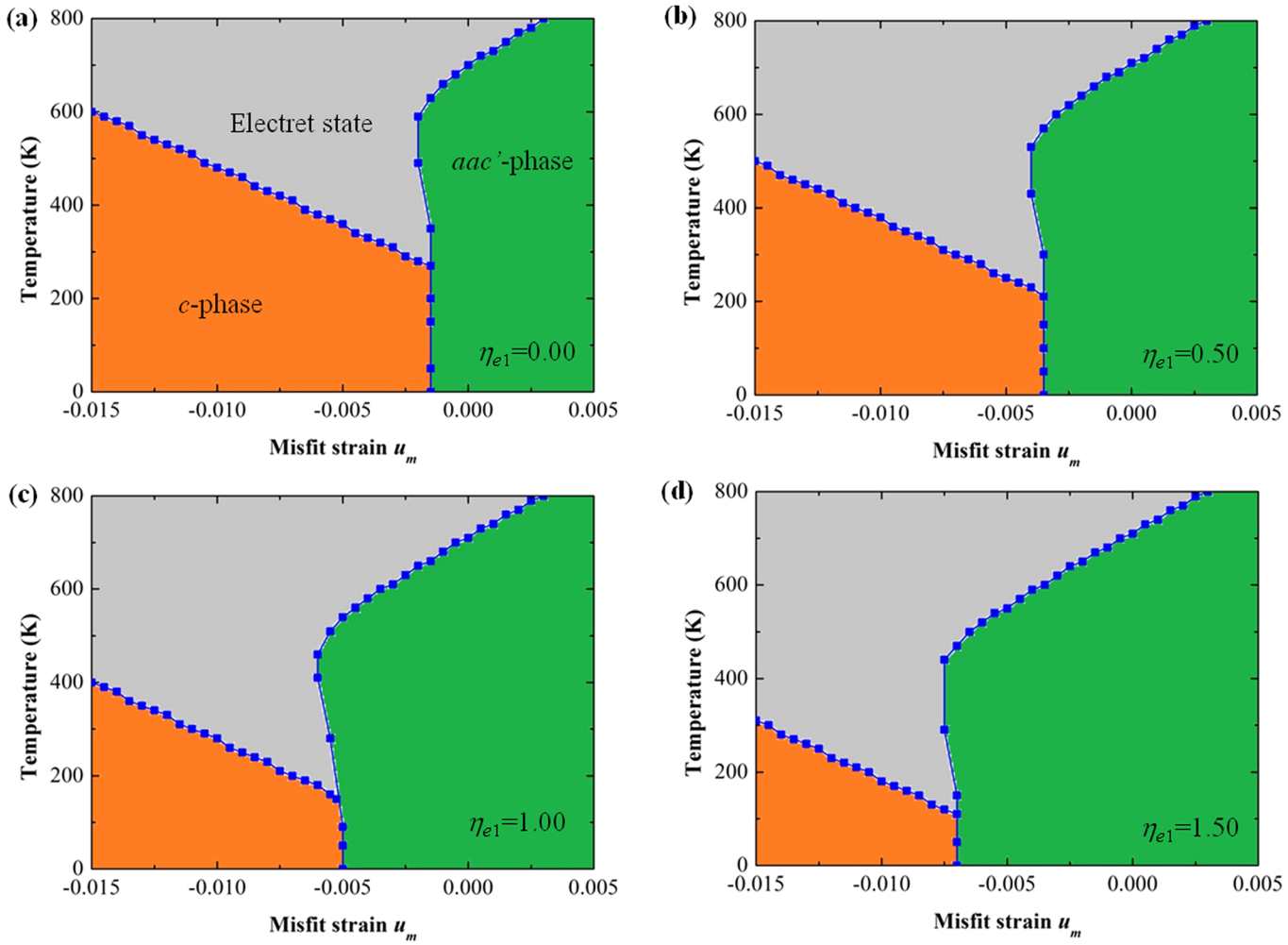

FIG. 5. Misfit strain-temperature phase diagram as a function of η_{e1} of asymmetric electrode-1/$PbTiO_3$/$SrRuO_3$ capacitor with 10 nm-thick $PbTiO_3$ thin film. (a) $\eta_{e1} = 0\,F^{-1}m^2$, (b) $\eta_{e1} = 0.50\,F^{-1}m^2$, (c) $\eta_{e1} = 1.00\,F^{-1}m^2$, and (d) $\eta_{e1} = 1.50\,F^{-1}m^2$.

that $\delta\varphi = 0.45$ V is the work function difference between the bulk Pt and bulk $SrRuO_3$electrodes.[20] In case of $\delta\varphi = 0$ V, from Fig. 2(a), it can be seen that the phase diagram of the capacitor is similar with those of the symmetric counterparts.[31] This phase diagram consists of paraelectric phase (p-phase), c-phase ($P_1 = P_2 = 0$, $P_3 \neq 0$), aa-phase ($P_1 = P_2 \neq 0$, $P_3 = 0$), and aac-phase ($P_1 = P_2 \neq 0$, $P_3 \neq 0$). However, as $\delta\varphi$ takes nonzero values, the phase diagram becomes dramatically different. In this case, the most distinct feature is that polarization states with nonzero P_3 component in parallel with the built-in field are preferential to form. Consequently, it is necessary to redefine phases with respect to the bistability of out-of-plane polarization. For example, as shown in Fig. 2(b) in case of $\delta\varphi = 0.15$ V, there are three phases in the phase diagram, i.e., the electret-state ($P_1 = P_2 = P_{3+} = 0$, $P_{3-} \neq 0$), c-phase ($P_1 = P_2 = 0$, $P_{3+} \neq P_{3-} \neq 0$), and aac'-phase ($P_1 = P_2 \neq 0$, $P_{3-} \neq 0$, $P_{3+} = 0$). Note that the electret-state and c-phase are different in polarization bistability although both of the phases have nonzero out-of-plane polarization. Similarly, aac-phase and aac'-phase are different in their bistability of P_3 component. Comparing with Figs. 2(a) and 2(b), the relations between different phases (e.g., the p-phase and the electret state, and aa-phase and aac'-phase) can be clearly seen. From Figs. 2(c) and 2(d), we can also see that the magnitude of built-in field significantly affects the phase boundaries. In particular, increasing built-in field tends to expand the electret-state region and compress those of the other two phases. As a result, the built-in field shifts the electret-state/c-phase boundary to lower temperature, and shifts the electret-state/aac'-phase boundary (low temperature section) to positive misfit strain. Note that the c-phase/aac'-phase boundary is also shifted to positive misfit strain by the increasing built-in field.

To explain the effect of $\delta\varphi$, in Fig. 3 we re-plot the phase diagrams of $\delta\varphi = 0$ V (red circle lines) and $\delta\varphi = 0.45$ V (blue square lines), and calculate the free energy profiles of points A, B, C, D, and E along the line $u_m = -0.012$ with $T = 0$ K, 200 K, 400 K, 600 K, and 800 K as marked in the phase diagrams. The results are shown in the upper and lower insets for cases $\delta\varphi = 0$ V and $\delta\varphi = 0.45$ V, respectively. When $\delta\varphi = 0$ V, the energy profiles are symmetric with respect to P_3. As temperature increases, the energy profile changes from symmetric double-well shape (e.g., points A, B, and C) to symmetric single-well shape (e.g., points D and E). Meanwhile, the minimum position changes from $P_3 \neq 0$ to $P_3 = 0$, indicating a c-phase to p-phase transition. When $\delta\varphi = 0.45$ V, the

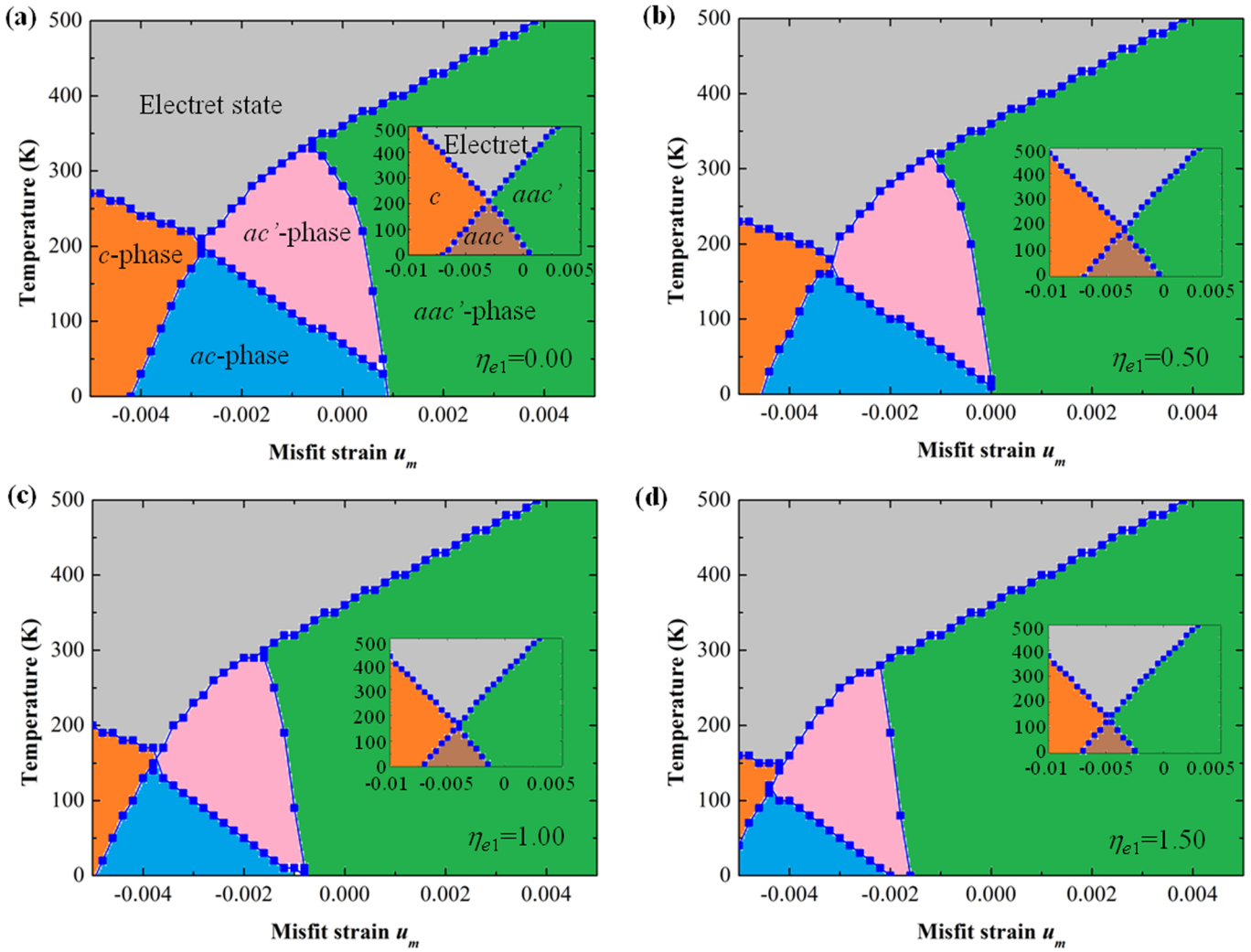

FIG. 6. Misfit strain-temperature phase diagram ($\mathbf{P}^6$ approximated potential) as a function of η_{e1} of asymmetric electrode-1/$BaTiO_3$/$SrRuO_3$ capacitor with 20 nm-thick $BaTiO_3$ thin film. (a) $\eta_{e1}=0\,F^{-1}m^2$, (b) $\eta_{e1}=0.50\,F^{-1}m^2$, (c) $\eta_{e1}=1.00\,F^{-1}m^2$, and (d) $\eta_{e1}=1.50\,F^{-1}m^2$. The inset figures depict the corresponding phase diagrams obtained by using the $\mathbf{P}^8$ approximated potential.

energy profiles are asymmetric due to the built-in electric field. At low temperatures, the energy profile has asymmetric double-well shape (e.g., points A and B), indicating that the system still has ferroelectric bistability. At high temperatures, the energy profile becomes asymmetric single-well shape (e.g., points C, D, and E), accompanying with a loss of ferroelectric bistability. Nevertheless, an out-of-plane polarization component is always induced as the minimum position of the single-well always departs from the zero point, leading to an electret-like ground state.

Using the $\mathbf{P}^6$ approximated potential, similar effects of built-in field are observed in the phase diagrams of $Pt/BaTiO_3/SrRuO_3$ capacitor with a 20 nm-thick $BaTiO_3$ thin film as shown in Fig. 4. It can be seen that in case of $\delta\varphi=0$ (see Fig. 4(a)), the capacitor has four phases, i.e., *p*-phase, *c*-phase ($P_1=P_2=0,\ P_3\neq 0$), *aa*-phase ($P_1=P_2\neq 0,\ P_3=0$), and *ac*-phase ($P_1\neq 0, P_2=0,\ P_3\neq 0$). As $\delta\varphi$ becomes nonzero, e.g., $\delta\varphi=0.15$ V as shown in Fig. 4(b), there are five phases in the phase diagram, i.e., the electret-state ($P_1=P_2=P_{3+}=0,\ P_{3-}\neq 0$), *c*-phase ($P_1=P_2=0,\ P_{3+}\neq P_{3-}\neq 0$), *ac*-phase ($P_1\neq 0, P_2=0,\ P_{3+}\neq P_{3-}\neq 0$), *ac*′-phase ($P_1\neq 0, P_2=P_{3+}=0,\ P_{3-}\neq 0$), and *aac*′-phase ($P_1=P_2\neq 0,\ P_{3-}\neq 0,\ P_{3+}=0$). Comparing the phase diagrams of $\delta\varphi=0$ V and $\delta\varphi=0.15$ V, the splitting of *ac*-phase into *ac*-phase and *ac*′-phase is clearly seen. From Figs. 4(b) to 4(d), it can be also seen that both the electret-state and the *ac*′-phase regions would expand as $\delta\varphi$ increases from 0.15 V to 0.45 V. As a result, a larger $\delta\varphi$ tends to shift down the electret-state/*c*-phase boundary and the *ac*′-phase/*ac*-phase boundary. Meanwhile, a larger $\delta\varphi$ also shifts the *ac*′-phase/*aac*′-phase boundary to positive misfit strain. Interestingly, the total boundary line which consists of the *c*-phase/*ac*-phase boundary, the electret-state/*aac*′-phase boundary, and the electret-state/*ac*′-phase boundary, is almost fixed at the same position. This is due to the fact that the built-in electric field mainly affects the relative stability of adjacent phases with different bistability of out-of-plane polarization. The inset figures in Figs. 4(a)–4(d) depict the corresponding phase diagrams of $BaTiO_3$ thin film using the $\mathbf{P}^8$ approximated potential. Note that the phase diagram of $\mathbf{P}^8$ approximated potential is different from that of $\mathbf{P}^6$ approximated potential. At $\delta\varphi=0$, the phase diagram consists of *p*-phase, *c*-phase, *aac*-phase, and *aa*-phase. Nevertheless, the effect of built-in field on the

phase diagram is similar. From the insets in Figs. 4(a) and 4(b), it can be seen that the nonzero built-in field changes the original *p*-phase and *aa* phase into electret-state and *aac′*-phase, respectively. Result also shows that increasing $\delta\varphi$ leads to the expansion of electret-state and *aac′*-phase regions in the phase diagrams of $\mathbf{P}^8$ approximated potential, accompanying with the shifting of the electret- state/*c*-phase boundary and the *aac*-phase/*aac′*-phase boundary.

In the following, we would like to investigate the influence of electrode screening on the misfit strain-temperature phase diagrams of the asymmetric capacitors. The phase diagrams of electrode-1/$PbTiO_3$/$SrRuO_3$ capacitor with the $PbTiO_3$ film thickness being 10 nm are shown in Fig. 5, where the screening parameter η_e of electrode-1 (i.e., η_{e1}) takes values of 0, 0.5, 1.0, and 1.5 $F^{-1}m^2$ and $\delta\varphi$ is fixed at 0.3 V. It can be seen that the phase boundaries of the system can be also strongly affected by the screening property of the electrodes. Similar with the effect of increasing built-in field, it can be seen in Fig. 5 that a larger η_e tends to compress the *c*-phase region, due to the depressing effect of depolarization field on *c*-phase. However, increasing η_e leads to expansion of the *aac′*-phase region, which is in contrast with the effect of increasing built-in field. Consequently, increasing η_e shifts the *c*-phase/*aac′*-phase boundary to negative misfit strain, and shifts the electret-state/*c*-phase boundary to lower temperature.

Using the $\mathbf{P}^6$ approximated potential, we further calculate the phase diagram as a function of screening parameter η_{e1} of electrode-1/$BaTiO_3$/$SrRuO_3$ capacitor with the $BaTiO_3$ film thickness being 20 nm, with the built-in field being fixed at 0.3 V. As shown in Fig. 6, similar effect of η_{e1} with that of $PbTiO_3$ system is observed. In particular, it can be seen that increasing η_{e1} from 0 to 1.5 $F^{-1}m^2$ causes a compression of *c*-phase, *ac*-phase, and *ac′*-phase regions, while it tends to expand the electret-state and *aac′*-phase regions. As a result, phase boundaries, such as the *ac*-phase/*ac′*-phase boundary and the *ac′*-phase/*aac′*-phase boundary, are shifted to lower temperature and negative misfit strain. Based on the $\mathbf{P}^8$ approximated potential, the corresponding phase diagrams of electrode-1/$BaTiO_3$/$SrRuO_3$ capacitor are also depicted in the insets of Figs. 6(a) to 6(d). It shows that the changing of η_{e1} leads to the shrinkage of *c*-phase and *aac*-phase region in a similar way with the effect of changing built-in field.

The dielectric constant ε_{33} as a function of misfit strain at room temperature of a Pt/$PbTiO_3$/$SrRuO_3$ capacitor with 10 nm-thick $PbTiO_3$ thin film is shown in Fig. 7(a). The inset in Fig. 7(a) also depicts the corresponding result of a Pt/$BaTiO_3$/$SrRuO_3$ capacitor with 20 nm-thick $BaTiO_3$ thin film at room temperature. Result shows that a smearing behavior of ε_{33} happens as $\delta\varphi$ changes into nonzero and the smearing peak slightly moves to the direction of positive misfit strain as $\delta\varphi$ increases. As is indicated by the vertical dotted lines, the smearing peak appears after the phase transition happens as the misfit strain increases. It can be seen that such a smearing behavior is a direct consequence of non-vanishing P_3 component. Fig. 7(b) also depicts smearing behavior of ε_{33} as a function of temperature for a Pt/$PbTiO_3$/$SrRuO_3$ capacitor with 10 nm-thick $PbTiO_3$ thin film at various $\delta\varphi$ and misfit strain u_m is fixed at −0.012. Similar result is found in the inset in Fig. 7(b) for a Pt/$BaTiO_3$/$SrRuO_3$ capacitor with 20 nm-thick $BaTiO_3$ thin film at misfit strain $u_m = -0.004$ using the $\mathbf{P}^6$ approximated potential.

B. Domain stability of asymmetric ferroelectric capacitors

From the above results obtained under single domain approximation, it can be seen that stability of out-of-plane polarization states is strongly affected by the built-in field. To further understand the distinct feature of asymmetric FCs from their symmetric counterparts, in the following we would like to investigate the stability of *c*-phase-domain structure in asymmetric FCs using the phase-field simulation method described in Sec. II B. We expect that polydomain pattern may become unstable as the film thickness decreases or temperature increases due to the fact that the built-in field significantly depresses the stability of out-of-plane polarization if its direction is opposite to the built-in field.

To see this, we simulate the polarization evolution to obtain the equilibrium domain patterns of Pt/$PbTiO_3$/$SrRuO_3$

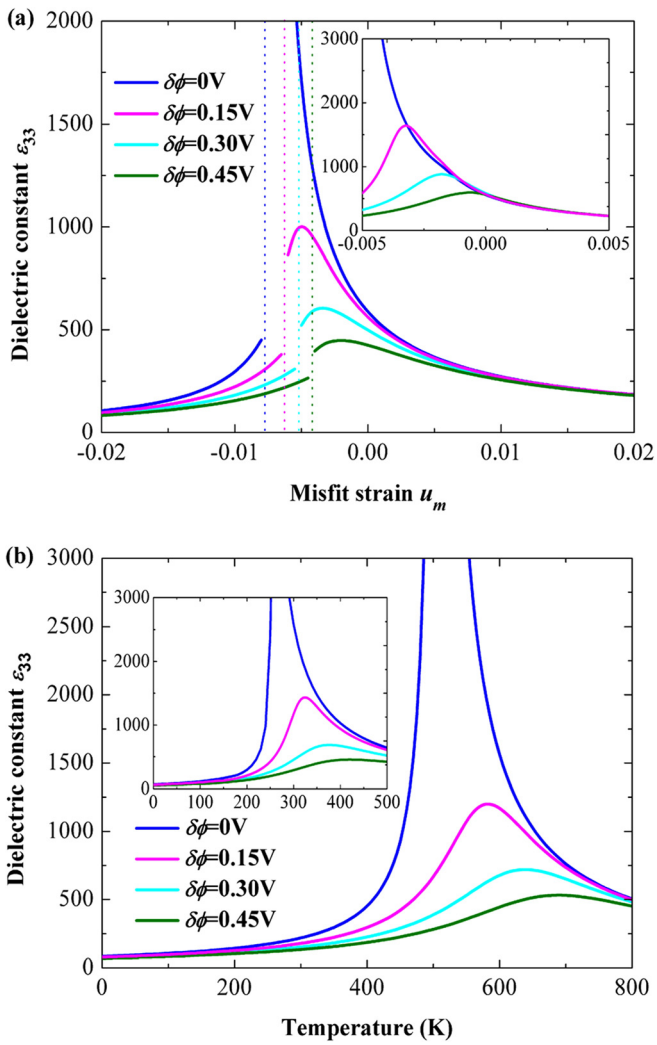

FIG. 7. Dielectric constant ε_{33} (a) as a function of misfit strain at room temperature and (b) as a function of temperature at $u_m = -0.012$ of asymmetric Pt/$PbTiO_3$/$SrRuO_3$ capacitor with 10 nm-thick $PbTiO_3$ thin film. The inset figures depict the corresponding results of asymmetric Pt/$BaTiO_3$/$SrRuO_3$ capacitor with 20 nm-thick $BaTiO_3$ thin film (a) at room temperature and (b) at $u_m = -0.004$.

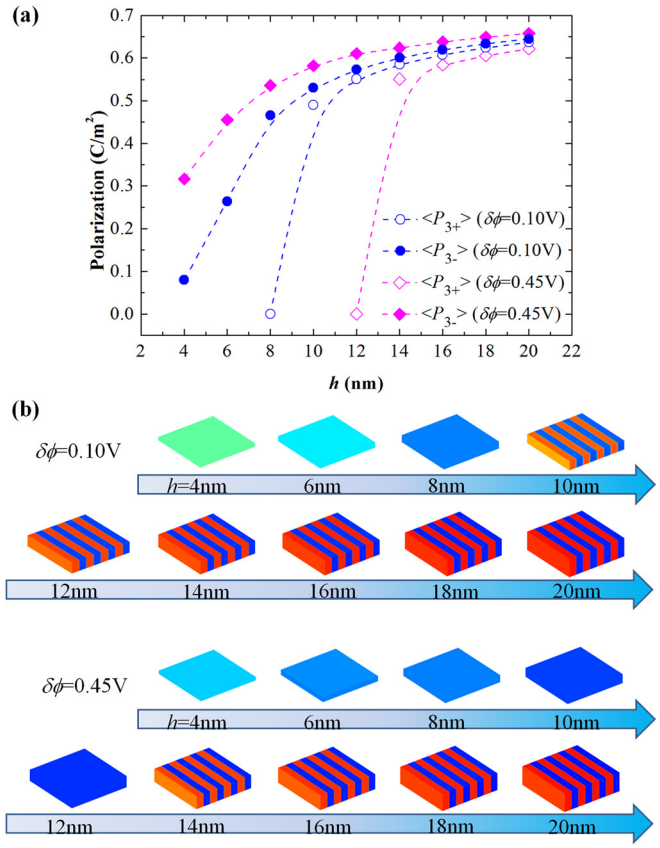

FIG. 8. Thickness dependence of (a) the average out-of-plane polarization in the two domain regions of the equilibrium domain pattern, i.e., $\langle P_{3+}\rangle$ and $\langle P_{3-}\rangle$, and (b) the corresponding domain morphologies in $Pt/PbTiO_3/SrRuO_3$ capacitors at room temperature, with a misfit-strain $u_m = -0.012$ and built-in field $\delta\varphi = 0.10$ V and 0.45 V. The initial domain patterns are 180° strip domains with domain width being 16 nm.

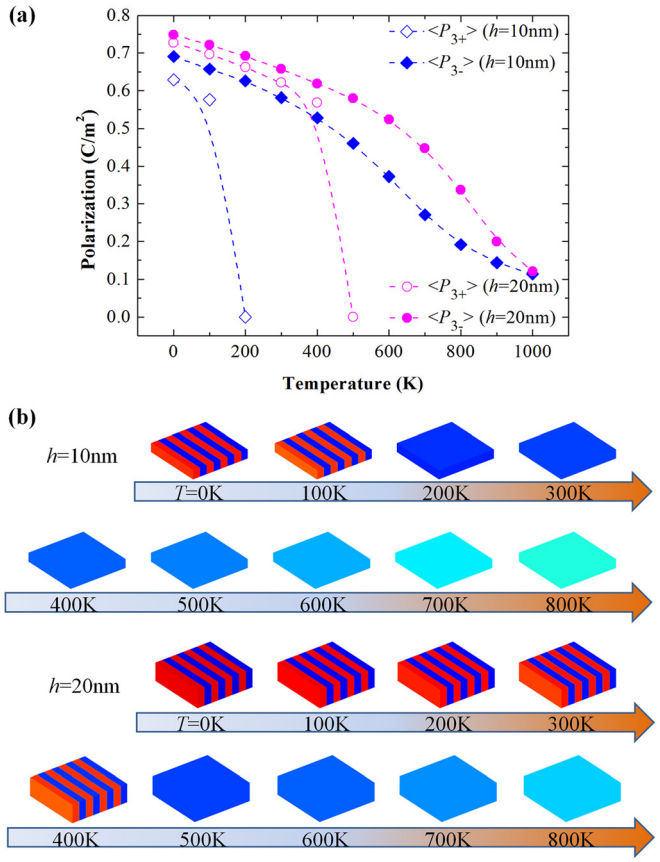

FIG. 9. Temperature dependence of (a) the average out-of-plane polarization in the two domain regions of the equilibrium domain pattern, i.e., $\langle P_{3+}\rangle$ and $\langle P_{3-}\rangle$, and (b) the corresponding domain morphologies in $Pt/PbTiO_3/SrRuO_3$ capacitors with film thickness being 10 nm and 20 nm at a misfit-strain $u_m = -0.012$ and built-in field $\delta\varphi = 0.45$ V. The initial domain patterns are 180° strip domains with domain width being 16 nm.

capacitors, which have initial polydomain patterns, i.e., 180° strip domain patterns with domain width being 16 nm. For capacitors at room temperature with a misfit strain $u_m = -0.012$ and built-in field $\delta\varphi = 0.45$ V, the film thickness dependence of the equilibrium domain pattern is shown in Fig. 8. To see the difference between the stability of P_{3+} domain and P_{3-} domain, in Fig. 8(a) we calculate the average out-of-plane polarization in the two domain regions of the equilibrium domain pattern, which is denoted as $\langle P_{3+}\rangle$ and $\langle P_{3-}\rangle$, respectively. It can be seen that capacitors with large film thickness maintain 180° strip domain patterns with $\langle P_{3+}\rangle$ smaller than $\langle P_{3-}\rangle$. As the film thickness decreases, both $\langle P_{3+}\rangle$ and $\langle P_{3-}\rangle$ decreases. However, the difference between their values becomes larger. A transition from polydomain (both $\langle P_{3+}\rangle$ and $\langle P_{3-}\rangle$ are nonzero) to monodomain (only $\langle P_{3-}\rangle$ is nonzero) happens as the film thickness decreases to 12 nm, indicating that the initial polydomain pattern is instable. This is also clearly seen in the domain morphologies (Fig. 8(b)). After transition, the monodomain pattern maintains a large $\langle P_{3-}\rangle$ even when the $PbTiO_3$ film thickness reaches down to 4 nm, which is likely to be an electret state. For $Pt/PbTiO_3/SrRuO_3$ capacitors with $\delta\varphi = 0.10$ V, the difference between the stability of P_{3+} domain and P_{3-} domain becomes smaller, and the transition thickness decreases to be 8 nm.

Fig. 9 also depicts the temperature dependence of the equilibrium domain pattern of $Pt/PbTiO_3/SrRuO_3$ capacitors with film thickness being 10 nm and 20 nm. The $PbTiO_3$ film is under a misfit strain $u_m = -0.012$ and a built-in field $\delta\varphi = 0.45$ V. Similar with the thickness effect, there is also a transition from polydomain (both $\langle P_{3+}\rangle$ and $\langle P_{3-}\rangle$ are nonzero) to monodomain (only $\langle P_{3-}\rangle$ is nonzero) as the temperature increases. After transition, the monodomain pattern maintains a large $\langle P_{3-}\rangle$ even when the temperature is much higher than the bulk Curie temperature (752 K), due to the forming of an electret state. The polydomain to monodomain transition temperature is about 200 K and 500 K for capacitors with film thickness being 10 nm and 20 nm, respectively, indicating a strong dependence of the transition temperature on film thickness.

C. Discussion

From the above results, it can be seen that asymmetric FCs indeed exhibit distinct misfit strain-temperature phase diagrams, dielectric property, and domain stability from symmetric counterparts and can be well adjusted by properties of the electrodes and interfaces. It should be pointed out that the presented results give us a qualitative rather than quantitative picture of related properties in asymmetric FCs. Actually, our investigation is rough one and may be regarded as "hard interface" model, where the properties of electrodes and interfaces, e.g., built-in field,

screening lengths, and extrapolation lengths, are treated as fixed external constraints on the energy minimization with respect to polarization. These properties are likely to be coupled with the polarization state of FTF (i.e., the interfaces are "soft" enough to be affected by the polarization).[18,19] Moreover, the interfacial structure and related properties may be sensitive to the strain state of the FTF and temperature. To obtain a more quantitative picture, all these features thus should be taken into account in the physical model. This may be done by introducing new order parameters to represent the change of interfacial structures and a modeling on the dependence of interfacial properties on the new order parameters, with the related coefficients determined by first-principle calculations and experiments. Nevertheless, this goes beyond the scope of the present work and will be done in a future study.

IV. CONCLUSIONS

In summary, we have investigated asymmetric electrodes controlling the misfit strain-temperature phase diagrams, dielectric property, and domain stability of asymmetric FCs using modified thermodynamic model and phase-field simulation. It is found that the misfit-strain temperature phase diagrams can be significantly affected by the work function steps difference between the interfaces and the screening properties of electrodes. Due to the intrinsic built-in electric field caused by the asymmetric interfaces, polar states with an out-of-plane polarization in parallel with the built-in field are always preferential to form. Meanwhile, the built-in field breaks the degeneracy of states with out-of-plane polarization in anti-directions. This leads to the necessity of redefining phases according to the bistability of out-of-plane polarization. Moreover, the phase boundaries can be significantly shifted by adjusting properties of electrodes. Result about the dielectric property also indicates promising controllability by electrodes, misfit-strain, and temperature. In addition, phase-field simulation result shows that due to the destroyed equivalence of two states with out-of-plane polarization in anti-directions, a polydomain to monodomain transition happens in asymmetric FCs as the film thickness decreases or temperature increases. These results should provide instructive information in applications of asymmetric FCs or FTJs.

ACKNOWLEDGMENTS

The authors gratefully acknowledge the financial support of NSFC (Nos. 51172291 and 11232015). Y. Zheng also thanks support by the Fundamental Research Funds for the Central Universities, NCET in University, Research Fund for the Doctoral Program of Higher Education, and Fok Ying Tung Foundation, Science and Technology Innovation Project of Guangdong Provincial Education Department and Guangdong Natural Science Funds for Distinguished Young Scholar.

[1]J. F. Scott, *Ferroelectric Memories* (Springer-Verlag, Berlin, 2000).
[2]M. Y. Zhuravlev, R. F. Sabirianov, S. S. Jaswal, and E. Y. Tsymbal, Phys. Rev. Lett. **94**, 246802 (2005).
[3]E. Y. Tsymbal and H. Kohlstedt, Science **313**, 181 (2006).
[4]J. R. Contreras, H. Kohlstedt, U. Poppe, R. Waser, C. Buchal, and N. A. Pertsev, Appl. Phys. Lett. **83**, 4595 (2003).
[5]H. Kohlstedt, N. A. Pertsev, J. R. Contreras, and R. Waser, Phys. Rev. B **72**, 125341 (2005).
[6]Y. Zheng and C. H. Woo, Nanotechnology **20**, 075401 (2009).
[7]X. Luo, B. Wang, and Y. Zheng, ACS Nano **5**, 1649 (2011).
[8]S. Y. Yang, J. Seidel, S. J. Byrnes, P. Shafer, C. H. Yang, M. D. Rossell, P. Yu, Y. H. Chu, J. F. Scott, J. W. Ager, L. W. Martin, and R. Ramesh, Nat. Nanotechnol. **5**, 143 (2010).
[9]J. Junquera and P. Ghosez, Nature **422**, 506 (2003).
[10]N. Sai, A. M. Kolpak, and A. M. Rappe, Phys. Rev. B **72**, 020101(R) (2005).
[11]Y. Umeno, B. Meyer, C. Elsässer, and P. Gumbsch, Phys. Rev. B **74**, 060101R (2006).
[12]C.-G. Duan, R. F. Sabirianov, W.-N. Mei, S. S. Jaswal, and E. Y. Tsymbal, Nano Lett. **6**, 483 (2006).
[13]G. Gerra, A. K. Tagantsev, N. Setter, and K. Parlinski, Phys. Rev. Lett. **96**, 107603 (2006).
[14]G. Gerra, A. K. Tagantsev, and N. Setter, Phys. Rev. Lett. **98**, 207601 (2007).
[15]A. K. Tagantsev, G. Gerra, and N. Setter, Phys. Rev. B **77**, 174111 (2008).
[16]M. Stengel, D. Vanderbilt, and N. A. Spaldin, Nature Mater. **8**, 392 (2009).
[17]M. Q. Cai, Y. Zheng, P. W. Ma, and C. H. Woo, J. Appl. Phys. **109**, 024103 (2011).
[18]M. A. M. Polanco, I. Grinberg, A. M. Kolpak, S. V. Levchenko, C. Pynn, and A. M. Rappe, Phys. Rev. B **85**, 214107 (2012).
[19]W. J. Chen, Y. Zheng, X. Luo, B. Wang, and C. H. Woo, J. Appl. Phys. **114**, 064105 (2013).
[20]N. A. Pertsev and H. Kohlstedt, Phys. Rev. Lett. **98**, 257603 (2007).
[21]Y. Zheng, M. Q. Cai, and C. H. Woo, Acta Mater. **58**, 3050 (2010).
[22]Y. Zheng, W. J. Chen, C. H. Woo, and B. Wang, J. Phys. D **44**, 095401 (2011).
[23]Y. Zheng, W. J. Chen, X. Luo, B. Wang, and C. H. Woo, Acta Mater. **60**, 1857 (2012).
[24]D. D. Fong, G. B. Stephenson, S. K. Streiffer, J. A. Eastman, O. Auciello, P. H. Fuoss, and C. Thompson, Science **304**, 1650 (2004).
[25]D. J. Kim, J. Y. Jo, Y. S. Kim, Y. J. Chang, J. S. Lee, J. G. Yoon, T. K. Song, and T. W. Noh, Phys. Rev. Lett. **95**, 237602 (2005).
[26]D. D. Fong, A. M. Kolpak, J. A. Eastman, S. K. Streiffer, P. H. Fuoss, G. B. Stephenson, C. Thompson, D. M. Kim, K. J. Choi, C. B. Eom, I. Grinberg, and A. M. Rappe, Phys. Rev. Lett. **96**, 127601 (2006).
[27]D. A. Tenne, P. Turner, J. D. Schmidt, M. Biegalski, Y. L. Li, L. Q. Chen, A. Soukiassian, S. Trolier-McKinstry, D. G. Schlom, X. X. Xi, D. D. Fong, P. H. Fuoss, J. A. Eastman, G. B. Stephenson, C. Thompson, and S. K. Streiffer, Phys. Rev. Lett. **103**, 177601 (2009).
[28]N. A. Pertsev, A. G. Zembilgotov, and A. K. Tagantsev, Phys. Rev. Lett. **80**, 1988 (1998).
[29]M. D. Glinchuk, A. N. Morozovska, and E. A. Eliseev, J. Appl. Phys. **99**, 114102 (2006).
[30]Y. L. Li, S. Y. Hu, Z. K. Liu, and L. Q. Chen, Appl. Phys. Lett. **78**, 3878 (2001).
[31]W. J. Chen, Y. Zheng, and B. Wang, Appl. Phys. Lett. **98**, 222902 (2011).
[32]C. H. Woo and Y. Zheng, Appl. Phys. A: Mater. Sci. Process. **91**, 59 (2008).
[33]Y. Zheng and C. H. Woo, Appl. Phys. A: Mater. Sci. Process. **97**, 617 (2009).
[34]Z. X. Zhu, J. F. Li, Y. Y. Liu, and J. Y. Li, Acta Mater. **57**, 4288 (2009).
[35]Y. Y. Liu, Z. X. Zhu, J. F. Li, and J. Y. Li, Mech. Mater. **42**, 816 (2010).
[36]A. N. Morozovska, E. A. Eliseev, S. V. Svechnikov, A. D. Krutov, V. Y. Shur, A. Y. Borisevich, P. Maksymovych, and S. V. Kalinin, Phys. Rev. B **81**, 205308 (2010).
[37]L. D. Landau, E. M. Lifshitz, and L. P. Pitaevskii, *Electrodynamics of Continuous Media* (Oxford University Press, Oxford, 1984).
[38]Y. Su and C. M. Landis, J. Mech. Phys. Solids **55**, 280 (2007).
[39]R. R. Mehta, B. D. Siilverman, and J. T. Jacobs, J. Appl. Phys. **44**, 3379 (1973).
[40]R. Kretschmer and K. Binder, Phys. Rev. B **20**, 1065 (1979).
[41]K. Ishikawa and T. Uemori, Phys. Rev. B **60**, 11841 (1999).
[42]Y. L. Li, L. E. Cross, and L. Q. Chen, J. Appl. Phys. **98**, 064101 (2005).
[43]In general, there may be a notable difference between ζ_{13} and ζ_{23}. Nevertheless, its effect is similar with the built-in field, and will not change the major conclusion.